Super-Resolution Hyperpolarized ^{13}C Imaging of Human Brain Using Patch-Based Algorithm

Junjie Ma[1] and Jae Mo Park[1,2,3]

[1]Advanced Imaging Research Center; [2]Department of Radiology, The University of Texas Southwestern Medical Center, Dallas, TX; and [3]Department of Electrical and Computer Engineering, The University of Texas at Dallas, Richardson, TX

Corresponding Author:
Jae Mo Park, PhD
The University of Texas Southwestern Medical Center,
5323 Harry Hines Blvd, Dallas, TX, 75390-8568;
E-mail: jaemo.park@utsouthwestern.edu

Key Words: Hyperpolarized 13C imaging, super-resolution, patch-based algorithm, human brain

Abbreviations: patch-based algorithm (PA), magnetic resonance (MR), spin-lattice relaxation time (T1), magnetic resonance spectroscopic imaging (MRSI), signal-to-noise ratio (SNR), magnetic resonance imaging (MRI), radiofrequency (RF), chemical shift imaging (CSI), sensitivity encoding (SENSE), fluid-attenuated inversion recovery (FLAIR), gray matter (GM), white matter (WM), cerebrospinal fluid (CSR), 2-dimensional (2D), sinc interpolation (SI), nearest-neighbor interpolation (NI), bilinear interpolation (BLI), spline interpolation (SP), region of interest (ROI), repetition time (TR), echo time (TE), field of view (FOV), LONI Probabilistic Brain Atlas (LPBA40), arterial spin labeling (ASL)

ABSTRACT

Spatial resolution of metabolic imaging with hyperpolarized ^{13}C-labeled substrates is limited owing to the multidimensional nature of spectroscopic imaging and the transient characteristics of dissolution dynamic nuclear polarization. In this study, a patch-based algorithm (PA) is proposed to enhance spatial resolution of hyperpolarized ^{13}C human brain images by exploiting compartmental information from the corresponding high-resolution ^{1}H images. PA was validated in simulation and phantom studies. Effects of signal-to-noise ratio, upsampling factor, segmentation, and slice thickness on reconstructing ^{13}C images were evaluated in simulation. PA was further applied to low-resolution human brain metabolite maps of hyperpolarized [1-^{13}C] pyruvate and [1-^{13}C] lactate with 3 compartment segmentations (gray matter, white matter, and cerebrospinal fluid). The performance of PA was compared with other conventional interpolation methods (sinc, nearest-neighbor, bilinear, and spline interpolations). The simulation and the phantom tests showed that PA improved spatial resolution by up to 8 times and enhanced the image contrast without compromising quantification accuracy or losing the intracompartment signal inhomogeneity, even in the case of low signal-to-noise ratio or inaccurate segmentation. PA also improved spatial resolution and image contrast of human ^{13}C brain images. Dynamic analysis showed consistent performance of the proposed method even with the signal decay along time. In conclusion, PA can enhance low-resolution hyperpolarized ^{13}C images in terms of spatial resolution and contrast by using *a priori* knowledge from high-resolution ^{1}H magnetic resonance imaging while preserving quantification accuracy and intracompartment signal inhomogeneity.

INTRODUCTION

Hyperpolarized ^{13}C magnetic resonance (MR) is an emerging imaging method that can assess *in vivo* metabolism (1). [1-^{13}C] pyruvate is currently the most widely used substrate for hyperpolarization and has proven its utility in exploring both normal and altered metabolism of multiple diseases with a series of successful translation to humans (2–5). Despite the relatively long spin-lattice relaxation time (T1) of [1-^{13}C] pyruvate, data acquisition with an adequate sampling rate is challenging for hyperpolarized ^{13}C imaging owing to the multidimensional nature of magnetic resonance spectroscopic imaging (MRSI) and the transient characteristics of hyperpolarized signals. Sufficient spectral bandwidth and resolution are needed to resolve ^{13}C-labeled products such as [1-^{13}C] lactate, [1-^{13}C] alanine, and [^{13}C] bicarbonate from hyperpolarized [1-^{13}C] pyruvate, and spatial encoding with proper k-space sampling is necessary to capture spatial distribution of the metabolites. In general, optimal acquisition strategies depend on the applications and adjust the tradeoffs between spectral, spatial, and time domains. In particular, compromised spatial resolution is inevitable owing to the limited signal-to-noise ratio (SNR) of hyperpolarized ^{13}C-labeled products, long acquisition time, and hardware performance. For instance, in-plane spatial resolution of cerebral metabolite maps in humans using hyperpolarized [1-^{13}C] pyruvate ranges from 1 cm to 2 cm (2, 3, 6, 7). The suboptimal resolution of hyperpolarized ^{13}C images usually results in large partial volume effects, hampering accurate assessment of the hyperpolarized metabolites. Exploiting the coregistered high-resolution structural ^{1}H magnetic

ISSN 2379-1381 https://doi.org/10.18383/j.tom.2020.00037

resonance imaging (MRI) for the reconstruction of hyperpolarized ^{13}C images may improve the spatial resolution, identifying the originated anatomical compartments of the hyperpolarized ^{13}C signal.

Several acquisition strategies have been suggested to improve spatial resolution of hyperpolarized ^{13}C images in the aspect of radiofrequency (RF) excitation and data sampling. A common approach is to omit the spectral sampling by applying a spectrally selective RF pulse, allowing more efficient utilization of hyperpolarized signals and longer acquisition time to cover larger k-space than conventional chemical shift imaging (CSI) methods (8). However, RF excitation with spectrally selective pulses is susceptible to potential contamination of other large hyperpolarized peaks, especially when imaging low-concentrated metabolites. Spectroscopic imaging sequences such as echo-planar spectroscopic imaging (9) or spiral CSI (10) can be also used to improve the spatial resolution at the expense of reduced spectral bandwidth. Besides, other conventional acceleration techniques such as parallel imaging (11) and compressed sensing (12) can be used in hyperpolarized ^{13}C imaging. Previous studies have shown 3-fold acceleration with 4-channel array coils using sensitivity encoding (SENSE) for hyperpolarized ^{13}C pyruvate spectroscopic imaging (13) and up to 3× acceleration using a volumetric echo-planar imaging in combination with compressed sensing for hyperpolarized [1-^{13}C] pyruvate and [1-^{13}C] lactate images (14). However, SNR penalty and possible artifacts exist when using these acceleration methods. Even with these techniques, the enhancement of spatial resolution for hyperpolarized ^{13}C images is still limited.

Spatial resolution can be also improved at the postprocessing level by the so-called super-resolution reconstruction methods (15). By definition, super-resolution methods reconstruct low-resolution images toward a higher spatial resolution under the guidance of *a priori* knowledge from other high-resolution imaging modalities without having any SNR penalty. For MRI, 2 types of super-resolution algorithms exist, namely, k-space-based and image-based methods (16). One type of k-space-based super-resolution method uses linear regression with an assumption of signal uniformity within each compartment, which is segmented by other high-resolution images. This type of method describes MR data as a linear combination of independent variables and solves the optimal weighting coefficients for the variables. For instance, spectral localization by imaging is a linear regression–based super-resolution method that uses structural information of ^{1}H spin-echo image to guide the reconstruction of MR spectroscopic data (17), allowing significant enhancement of spatial resolution of the spectroscopic image. The linear regression method can be further improved by adding a regularization function that constraints anatomical consistency (18). Recently, Farkash et al. (19) applied a modified linear algebraic model to hyperpolarized ^{13}C MRSI to enhance the spatial resolution of ^{13}C images with the assumption of spectra similarity within each compartment. Another type of k-space-based super-resolution method is Bayesian super-resolution method that formularizes the reconstruction as a likelihood function from the *a priori* structural information. The Bayesian method was used to reconstruct ^{1}H brain MRSI data by incorporating anatomical information from high-resolution magnetization–prepared rapid acquisition gradient-echo images (20). Although more accurate regional metabolite levels are quantifiable with the Bayesian-based method, often locally optimal solutions are found owing to the reconstruction complexity.

Image-based super-resolution method is a relatively simple alternative of k-space-based methods. In particular, patch-based algorithm (PA) is an image-based method that reconstructs a high-resolution image using the similarity of the adjacent voxels to the central voxel. The similarity is defined by the matching high-resolution reference images. As PA specifies only similarity of signal distribution, it still allows signal variability within the same compartment. Previously, PA was applied to reconstruct MRSI of patients with multiple sclerosis (16). In the study, low-resolution N-acetylaspartate and myo-inositol maps were upsampled under the guidance of ^{1}H T1-weighted and fluid-attenuated inversion recovery (FLAIR) images, which outperformed other conventional upsampling methods in preserving the structural information and the tissue contrasts.

One major challenge of implementing super-resolution methods is the choice of appropriate *a priori* knowledge; this usually comes from attendant high-resolution acquisition, physical principles related to the measurement process, or precepts from previous experience (15). Jain et al. (16) acquired *a priori* information from high-resolution ^{1}H T1-weighted and FLAIR images, which share the same brain tissue boundaries with the low-resolution MRSI. Previous healthy human brain imaging studies (2, 6) showed compartmentalized spatial distribution of hyperpolarized ^{13}C metabolites between gray matter (GM) and white matter (WM) even though the distribution of ^{13}C signals according to anatomic segmentation needs further investigation.

In this study, we propose a modified PA for enhancing the spatial resolution of hyperpolarized ^{13}C human brain images by using the brain tissue boundaries' information from high-resolution ^{1}H T1-weighted MRI. The effect of SNR, upsampling factor, segmentation, and slice thickness on the performance of PA is evaluated with digital phantoms, and the feasibility of the proposed method for reconstructing high-resolution ^{13}C images is shown in phantom studies and in vivo hyperpolarized [1-^{13}C] pyruvate images of healthy human brain.

METHODOLOGY

Patch-Based Super-Resolution Algorithm

For a low-resolution hyperpolarized ^{13}C image $\boldsymbol{y}$, the corresponding to-be-reconstructed high-resolution image $\boldsymbol{x}$ can be described as follows:

$$\boldsymbol{y} = \boldsymbol{H}\boldsymbol{x} + \boldsymbol{\eta} \tag{1}$$

where $\boldsymbol{H}$ is the blurring and downsampling operator, and $\boldsymbol{\eta}$ is the acquisition noise. To reconstruct $\boldsymbol{x}$, a classical smoothness constraint can be applied to the high-resolution image as follows:

$$\hat{\boldsymbol{x}} = \mathbf{argmin}\left\{ \|\boldsymbol{y} - \boldsymbol{H}\boldsymbol{x}\|^2 + \boldsymbol{\lambda}\boldsymbol{\Phi}(\boldsymbol{x}) \right\} \tag{2}$$

where $\boldsymbol{\Phi}(\boldsymbol{x})$ is the regularization term that maintains the geometric consistency of $\boldsymbol{x}$, and $\boldsymbol{\lambda}$ controls the level of the regularization. The regularization term is determined by the nonlocal patch–based method (21, 22) in the high-resolution space, $\boldsymbol{\Omega}$:

$$\Phi(x) = \sum_{i \in \Omega} \|x_i - \psi(x_i|V_i)\|^2 \quad (3)$$

$\psi(x_i|V_i)$ is the estimated value of x_i, calculated from the neighboring voxels within the volume, V_i. For ^{13}C MRSI, patches from different metabolites are assumed to be similar. Moreover, as the spatial resolution increases, the similarities between neighboring patches are expected to decrease. Under these assumptions, the 2 terms in equation [2] can be decoupled and separately calculated during the mean correction and reconstruction steps, respectively (16), and λ can be ignored, as the 2 terms are asymptotically approximated.

$\psi(x_i|V_i)$ is defined as follows:

$$\psi(x_i|V_i) = \sum_{j \in V_i} w(x_i, x_j) x_j \quad (4)$$

The weighting factor, $w(x_i, x_j)$, quantifies the contribution of voxel, x_j, to the reconstruction of x_i based on *a priori* knowledge (23):

$$w(x_i, x_j) = \frac{1}{Z_i} e^{-\frac{\|\hat{N}_i - \hat{N}_j\|^2}{2\sigma_i^2}} \quad (5)$$

Z_i is the normalization constant that satisfies $\frac{1}{Z_i}\sum_{j \in V_i} w(x_i, x_j) = 1$. $\hat{N}_i$ and $\hat{N}_j$ are the intensity matrices of the neighborhood voxels around voxel i and j, respectively. σ_i^2 is the variance of the neighborhood voxel intensities in $\hat{N}_i$. In this study, $\hat{N}_i$ and $\hat{N}_j$ are both 5×5 matrices.

A previous study (24) proposed a PA that conducts nonlocal means reconstruction iteratively using equation [4] (reconstruction step). For each iteration, the offset between the reconstructed values and the acquired low-resolution data is adjusted (mean correction step). The corrected signal intensity of voxel i is as follows:

$$x_i' = x_i - U(y - H(x_i)) \quad (6)$$

where U is an upsampling operator. In this study, the downsampling operation, H, is conducted by averaging signal from corresponding voxels at high resolution. As an extension of equation [5], the weighting factors can include tissue compartmentalization, estimated from other types of images (16):

$$w_{^1H}(x_i, x_j) = \frac{1}{Z_i \cdot K} \sum_k^K p_{i,k} \cdot p_{j,k} \cdot e^{-\frac{\|\hat{N}_i - \hat{N}_j\|^2}{2\sigma_i^2}} \quad (7)$$

Here, k specifies individual tissue compartment ($k \in K$), and $p_{i,k}$ is the probability that voxel i belongs to compartment k. In this preliminary study, we considered 3 compartments in the brain: K = (GM, WM, cerebrospinal fluid [CSF]) using a high-resolution T1-weighted ^{1}H MRI.

Figure 1 shows the schematic diagram of PA for reconstructing high-resolution hyperpolarized ^{13}C images. High-resolution ^{1}H MRI (eg, T1-weighted ^{1}H MRI) and low-resolution hyperpolarized ^{13}C MRI, acquired from the same subject, are used as input. Then, 3 compartments (WM, GM, CSF) are segmented from the T1-weighted ^{1}H image to get the possibility maps and the ^{1}H MRI weights. As an initial step, the low-resolution hyperpolarized ^{13}C image is upsampled to the targeted spatial resolution. Using the ^{1}H MRI weights, the previously estimated high-resolution ^{13}C image is updated, followed by a mean correction step. These iterative steps continue until the maximum signal difference of all voxels between the previous iteration and current iteration is smaller than a threshold. The final super-resolution hyperpolarized ^{13}C MRI is used to evaluate the proposed PA.

Hardware and Hyperpolarization

All the MR studies were performed using a clinical 3 T 750w wide-bore MRI scanner (diameter ∅ = 70 cm; GE Healthcare, Waukesha, WI). A ^{1}H/^{13}C dual-tuned quadrature transmit/receive birdcage RF coil ($\varnothing_{inner}$ = 60 mm; GE Healthcare) was used for phantom studies. Human brain imaging was performed using a dual-frequency human head RF coil (nested-design of a quadrature transmit/receive ^{1}H coil, quadrature ^{13}C transmit coil, and 8-channel ^{13}C array receive coils) (25). For in vivo studies, [1-^{13}C] pyruvic acid samples (Sigma Aldrich, St. Louis, MO) were prepared in clinical fluid paths and polarized using a SPINlab™ clinical dynamic nuclear polarization system (GE Healthcare) as described previously (5). The imaging protocol was approved by the local institutional review board (IRB#: STU 072017-009).

Simulation

A series of simulations were performed using digital phantoms to evaluate the effects of SNR, upsampling factor, segmentation, and slice thickness on the performance of the proposed algorithm. All the digital phantoms were generated using MATLAB (MathWorks, Natick, MA). A 2-dimensional (2D) phantom image consisting of 3 compartments (matrix size = 64×64) was used as a high-resolution ^{1}H MRI (Figure 2A), and the possibility map of each compartment was calculated. Similarly, 2 low-resolution images were created for ^{13}C MRI with peak SNRs (SNR_{peak}) of 10 and 100 (matrix size = 16×16; Figure 2B). The mean ^{13}C signal intensities of compartments 1, 2, and 3 were assigned to 1000, 750, and 250, respectively. From the high-resolution ^{1}H image and the low-resolution ^{13}C images, high-resolution ^{13}C images were reconstructed using PA. For comparison, conventional interpolation methods, including sinc interpolation (SI), nearest-neighbor interpolation (NI), bilinear interpolation (BLI), and spline interpolation (SP), were applied to the low-resolution ^{13}C images. The SI method interpolates the image data by zero-filling the high spatial-frequency components of the k-space data. The NI method assigns the query point to the value of the nearest sample grid point. The BLI method linearly interpolates the new point based on the nearest 2-by-2 neighborhood. For SP, a cubic spline method was used to interpolate the new point with 4 old points in the neighborhood. The mean signal intensities from 4 region of interests (ROIs), drawn in different compartments of the low-resolution ^{13}C images, were used as ground truth.

To consider the cases of inaccurate segmentation from high-resolution ^{1}H MRI, 2 additional low-resolution ^{13}C images were generated (matrix size = 16×16, SNR_{peak} = 10): one with an extra ^{13}C signal source in a segmented compartment (Figure 3) and the other with missing ^{13}C signal in a compartment (Figure 4). The signal intensities of these 2 images were maintained the same as before (1000, 750, and 250).

The effect of slice thickness on the performance of PA was determined using a 3D digital phantom with 3 compartments.

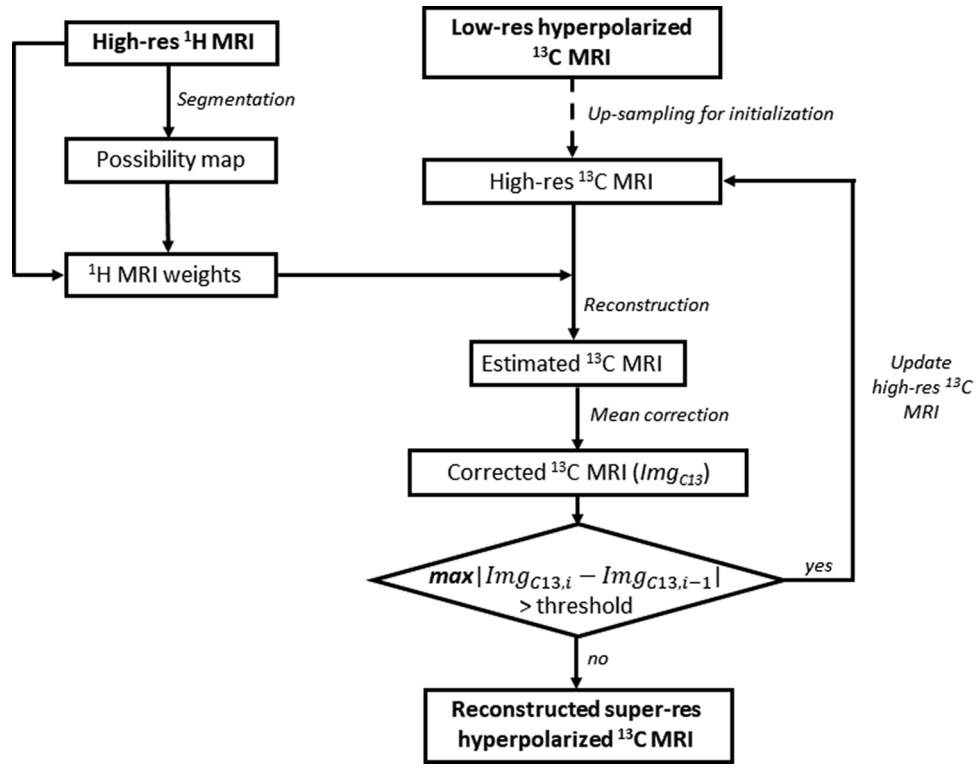

Figure 1. Schematic diagram of the patch-based super-resolution reconstruction algorithm for hyperpolarized ^{13}C magnetic resonance imaging (MRI).

Six slices were generated for ^{1}H MRI (simulated slice thickness = 5 mm, matrix size = 64 × 64). For ^{13}C images, 2 cases of slice thicknesses were simulated (2, 3, 6, 7). In the first case, 2-slice low-resolution ^{13}C MRIs were generated with SNR_{peak} = 6.67 and SNR_{peak} = 10 (simulated slice thickness = 1.5 cm, matrix size = 16 × 16; Figure 5B). In the second case, single-slice low-resolution ^{13}C image was generated (simulated slice thickness = 3.0 cm, matrix size = 16 × 16; Figure 5C). The SNR_{peak} of the single slice was 16.67. For each 5-mm slice, the ^{13}C signal intensities in compartments 1, 2, and 3 were assigned as 1000, 750, and 250, respectively.

Phantom Validation

Four cylindrical phantoms (Figure 6; ∅ = 1 cm, length = 5 cm) were prepared for performance evaluation of PA at the scanner. Phantoms #1–#3 were filled with pure ethylene glycol (not ^{13}C-labeled) with concentration of 17.7, 13.3, and 8.8 M, respectively. Phantom #4 was filled with water. The corresponding high-resolution ^{1}H MRI was acquired with 2D T1-weighted fast spin echo sequence (repetition time [TR] = 114 millisecond, echo time [TE] = 42 millisecond, flip angle = 90°, field of view [FOV] = 60 × 60 mm^2, slice thickness = 10 mm, spatial resolution = 0.23 × 0.23 mm^2, number of averages = 3). For ^{13}C imaging, free induction decay CSI sequence was used (TR = 3000 millisecond, flip angle = 90°, FOV = 60 × 60 mm^2, slice thickness = 10 mm, nominal spatial resolution = 5 × 5 mm^2, number of averages = 32). The acquired low-resolution ^{13}C image was reconstructed to 3 different spatial resolutions (2.5 × 2.5 mm^2, 1.25 × 1.25 mm^2, and 0.625 × 0.625 mm^2) using PA, and the reconstructed results were compared with the interpolated images by SI, NI, BLI, and SP methods.

In Vivo Human Brain Study

Brain images were acquired from a healthy volunteer (63-year-old, male) using a brain MR protocol, which includes a series of ^{1}H imaging and an injection of hyperpolarized [1-^{13}C] pyruvate, followed by a 2D dynamic spiral CSI (FOV = 24 × 24 cm^2, matrix size = 16 × 16, slice thickness = 2–3 cm, variable flip angle up to 30° each time point, TR = 5 seconds, 7 spatial interleaves in spiral readout, spectral width = 814 Hz, number of echoes = 48, number of dynamic acquisitions = 16) (26, 27). Polarization level and concentration of the pyruvate solution measured by the quality control device (GE Healthcare) were 36.5% and 234mM, respectively. For the ^{1}H imaging, 2D axial T1-weighted FLAIR and T2-weighted fast spin echo scans were conducted (slice thickness = 0.5 cm, number of slices = 14). The hyperpolarized [1-^{13}C] pyruvate solution passed the quality control before the injection. In total, 80 seconds after the dissolution, a dose of 0.1 mmol/kg of hyperpolarized pyruvate solution was administered intravenously to the subject, followed by a 25-mL saline flush (injection rate = 5 mL/s). The ^{13}C acquisition began 3 seconds after the start of injection, and the center frequency was set to the in vivo hyperpolarized [1-^{13}C] pyruvate resonance. The acquired ^{1}H images were used for brain skull-stripping and brain segmentation with FSL package (FMRIB, Oxford, UK) (28, 29), from which the possibility maps of GM, WM, and CSF were produced. The ^{13}C data were reconstructed using MATLAB, and the time-averaged images of hyperpolarized [1-^{13}C] pyruvate and [1-^{13}C] lactate were upsampled by 2 and 4 times using the 5 interpolation methods (SI, NI, BLI, SP, and PA). Besides, the kinetic results of [1-^{13}C] pyruvate and [1-^{13}C] lactate from different reconstruction methods were compared.

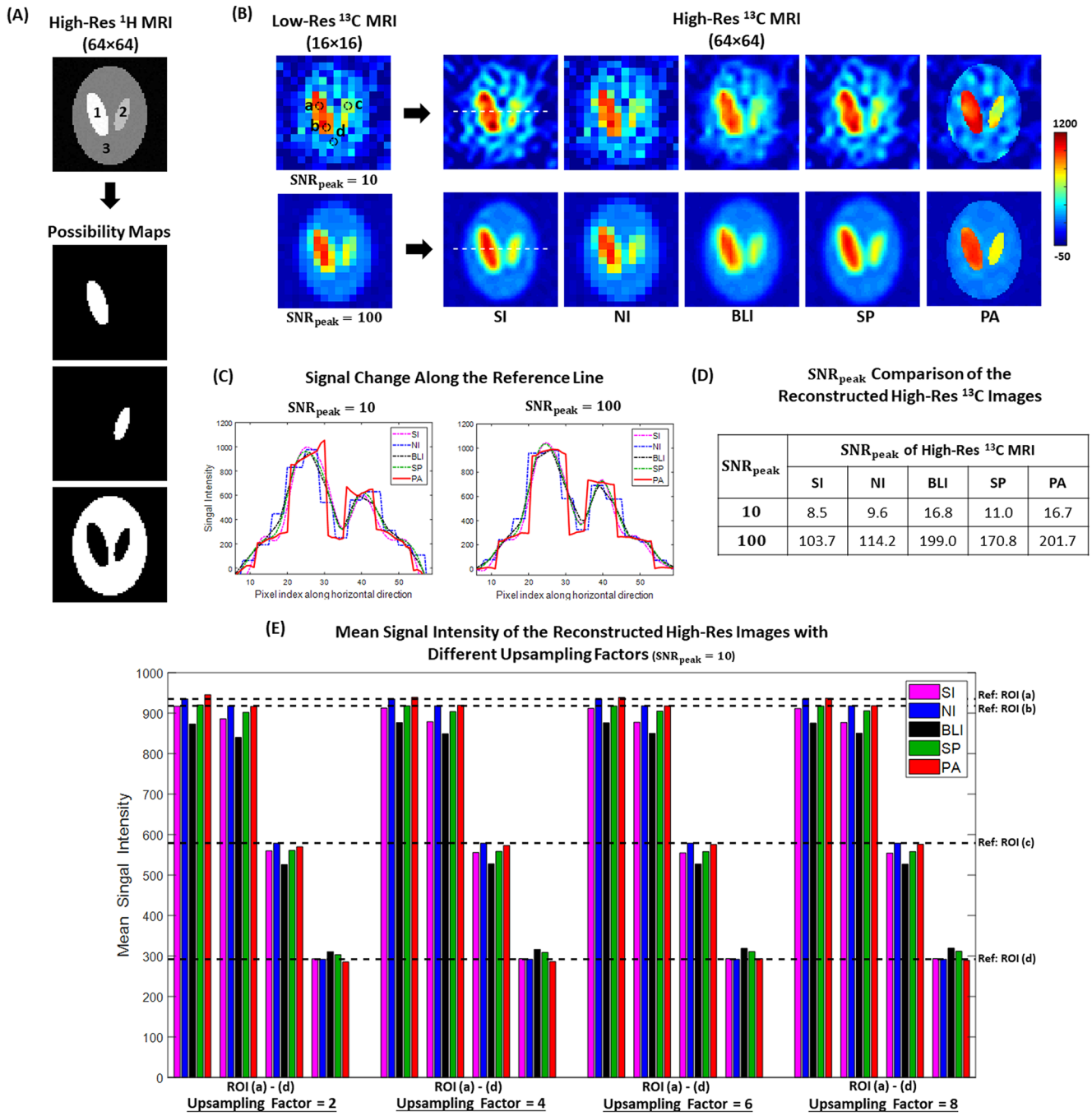

SNR_{peak}	SNR_{peak} of High-Res ^{13}C MRI				
	SI	NI	BLI	SP	PA
10	8.5	9.6	16.8	11.0	16.7
100	103.7	114.2	199.0	170.8	201.7

Figure 2. Simulation results when ^{1}H-based possibility maps are aligned with ^{13}C distribution. Possibility maps of the 3 compartments were calculated from a high-resolution ^{1}H digital phantom (A). Low-resolution ^{13}C images with signal-to-noise ratio $(SNR)_{peak}$ = 10 (top) and 100 (bottom) were upsampled by 4 times using sinc interpolation (SI), nearest-neighbor interpolation (NI), bilinear interpolation (BLI), spline interpolation (SP), and patch-based algorithm (PA) (B). High-resolution ^{13}C images by PA showed increased contrast along the reference lines (dotted lines in B) (C) and improved SNR as compared with the other methods for both low- and high-SNR cases (D). Mean signal intensities of region of interests (ROIs) (dotted circles in B) in the reconstructed high-resolution ^{13}C images with upsampling factors of 2, 4, 6, and 8 (E).

RESULTS

When the ^{1}H-based segmentation was correctly assigned to the ^{13}C signal distribution, PA reconstructed high-resolution ^{13}C images with enhanced spatial resolution and contrast (Figure 2). The high-resolution ^{13}C images that were reconstructed using PA outperformed those reconstructed by SI, NI, BLI, and SP methods (Figure 2B) with respect to the contrast at the edge of each compartment. Both low- and high-SNR ^{13}C images (SNR_{peak} = 10 and

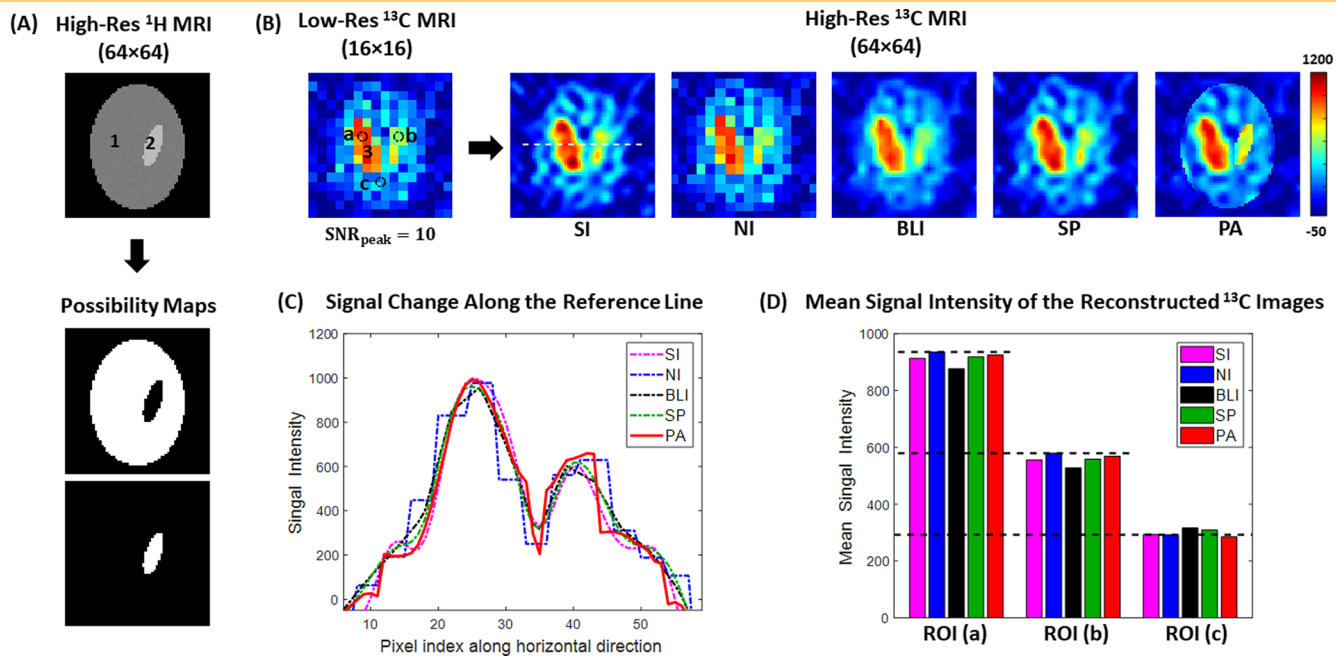

Figure 3. Simulation results when an extra ^{13}C signal source with distinct signal intensity exists in a segmented compartment. Two possibility maps were derived from the simulated high-resolution ^{1}H MRI, which did not show the compartment #3 (A). High-resolution ^{13}C images were reconstructed using SI, NI, BLI, SP, and PA (B). The signal changes along the reference line (dotted line in B) (C) and the quantification result from different ROIs (dotted circles in B) (D) are summarized.

100) confirmed the sharper transition of signal intensity between compartments and more consistent signal profiles within each compartment, as shown by the cross-sectional profiles along the reference lines (Figure 2C). The peak SNRs from the reconstructed images were quantified and summarized in Figure 2D. Along with BLI and SP, PA moderately improved the SNR. The mean signal intensities calculated from the 4 ROIs (SNR$_{peak}$ = 10) showed that PA maintains the quantification accuracy in the reconstructed high-resolution ^{13}C images for upsampling factors of 2–8 (Figure 2E). Moreover, signal variation within each compartment was preserved by PA for the tested upsampling factors, particularly for ROI (a) and (b). The simulation validated reliability of the proposed method when the compartments were properly segmented to the ^{13}C distribution.

Performance of PA was further tested when ^{13}C signal distribution and segmentation were mismatched. First, the case when an additional ^{13}C signal source presents within one of the ^{1}H-defined possibility maps was examined. When compartment #3 of the simulated low-resolution ^{13}C image was not identified by the ^{1}H image (Figure 3A), compartment #3 was treated as a part of compartment #2 in the possibility maps, although the compartments showed distinct ^{13}C signal intensities. In this case, all the conventional methods (SI, NI, BLI, and SP) retained the structural information of the 3 compartments in the interpolated images (Figure 3B). The reconstructed image by PA also showed comparable signal distribution in the unsegmented compartment (compartment #3) while achieving enhanced contrasts compared with other interpolation methods in the properly segmented compartments (compartments #1 and #2) as shown in the cross-sectional profile (Figure 3C) along the reference line (white dotted line in Figure 3B). PA was able to maintain the quantification accuracy in the missing compartment (Figure 3D). Second, PA was tested for the case when a compartment in the ^{13}C map is partially lost (eg, signal contamination owing to noise, shading, or artifacts). To show the case, a low-resolution ^{13}C phantom image with partially lost signal from the upper part of compartment #3 was generated (Figure 4), whereas the ^{1}H image showed homogeneous signal distribution within the compartment. All the interpolation methods, including PA, showed clear boundaries between upper and lower parts of the compartment #3 (Figure 4B), and the signal distribution along the reference line x was at the noise level (Figure 4C). Meanwhile, PA still outperformed the conventional interpolation methods in terms of contrast (Figure 4, B and D).

The effect of relative ^{13}C/^{1}H slice thickness on PA reconstruction was also evaluated. A 3D 3-compartment digital phantom was created for high-resolution ^{1}H MRI (6 slices, simulated slice thickness = 0.5 cm; Figure 5A). From the corresponding thicker low-resolution ^{13}C images (2 slices, simulated slice thickness = 1.5 cm), the matching 2-slice possibility maps were calculated (Figure 5B). When PA was applied to the low-resolution ^{13}C images with the possibility maps and an upsampling factor of 4, enhanced contrast across the compartments was observed in both slices. Quantification accuracy was also comparable to that from other interpolation methods for both slices. Similarly, the reconstructed high-resolution images from a thicker ^{13}C image (single slice, simulated slice thickness = 3.0 cm; Figure 5C) also showed moderately enhanced contrast and comparable signal distribution when PA was applied as compared with the other

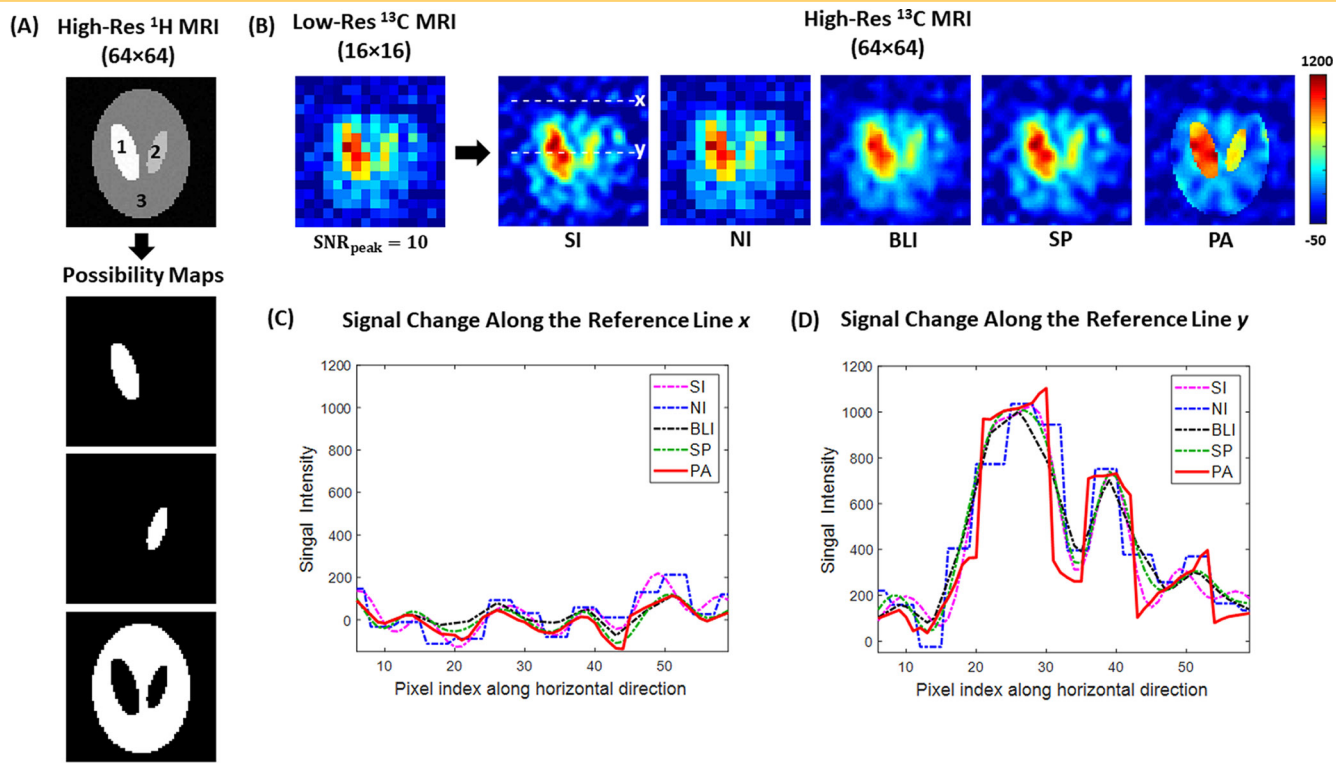

Figure 4. Simulation results when ^{13}C signal is partially missing in a compartment. Three possibility maps were calculated from the high-resolution ^{1}H digital phantom (A). A low-resolution ^{13}C MRI was created to have diminishing ^{13}C signal in the upper part in compartment #3 and upsampled to high-resolution ^{13}C images using SI, NI, BLI, SP and PA (B). The signal changes along the reference lines *x* (C) and *y* (D) (dotted lines in B) are summarized.

methods. It was noted that the contrast enhancement in reconstructed image by PA was reduced when the ^{13}C slice thickened.

Figure 6 shows the phantom test results at the scanner. A low-resolution ^{13}C image was obtained from the 4 cylindrical tubes that contain incremental concentrations of ethylene glycol (spatial resolution = $5 \times 5mm^2$; Figure 6B). High-resolution ^{13}C images were reconstructed using SI, NI, BLI, SP, and PA with upsampling factors of 2, 4, 6, and 8, respectively. Figure 6, B and C, shows the reconstructed high-resolution ^{13}C images and the signal change along the reference lines *x*, *y*, and *z* with an upsampling factor of 4 (spatial resolution= $1.25 \times 1.25\ mm^2$). The high-resolution image from PA showed significantly enhanced contrast as compared with the results from the other interpolation methods. In all of the upsampled images, no obvious ^{13}C signal was detected from the water phantom (phantom #4). The mean signal intensities calculated from 3 ROIs of the reconstructed high-resolution images are summarized in Figure 6D, which shows accurate quantification results from PA compared with the ground truth.

Finally, the proposed super-resolution method was tested with hyperpolarized ^{13}C human brain images. After skull-stripping from the T1-weighted ^{1}H image, the possibility maps of GM, WM, and CSF were calculated (Figure 7A). The time-averaged low-resolution hyperpolarized ^{13}C images of [1-^{13}C] pyruvate and [1-^{13}C] lactate (spatial resolution = $1.5 \times 1.5cm^2$) were upsampled by 2 and 4 times using SI, NI, BLI, SP, and PA. Peak SNR was measured as 32.4 and 20.9 from the pyruvate and lactate images, respectively. Figure 7B shows the 4-fold upsampled hyperpolarized ^{13}C images, overlaid over the corresponding ^{1}H MRI (spatial resolution = $0.375 \times 0.375cm^2$). Compared with the upsampled images using SI, NI, BLI, and SP, the results from PA showed clearer boundaries for each compartment. In particular, the edge of brain and the boundary across CSF and WM showed significant contrast enhancement. The signal changes along the reference lines (dotted lines in Figure 7B) are shown in Figure 7D, and again, the upsampled images from PA showed the highest contrast at the edge and similar intracompartment signal profile as other images. Moreover, signal increased at the edge of the brain in PA-reconstructed ^{13}C images, especially in the pyruvate map. The mean signal intensities from ROIs in CSF (ROI 1), GM (ROI 2), and WM (ROI 3) are summarized in Figure 7F. For all 3 ROIs, the quantification accuracy of mean signal intensities was comparable between PA and the other methods for both 2- and 4-time upsampled cases.

Figure 8 shows the time-resolved low-resolution images of hyperpolarized [1-^{13}C] pyruvate and [1-^{13}C] lactate at selected time points and the interpolated high-resolution images. Similar to the time-averaged images, increased contrast was consistently observed after applying PA even with the decaying ^{13}C SNRs over time. Temporal changes in 3 representative ROIs of CSF (#1), GM (#2), and WM (#3) were comparable to those from other interpolation methods (Figure 8C). For full ^{13}C images of pyruvate and lactate at all time points and the averaged spectrum, see online supplemental Material.

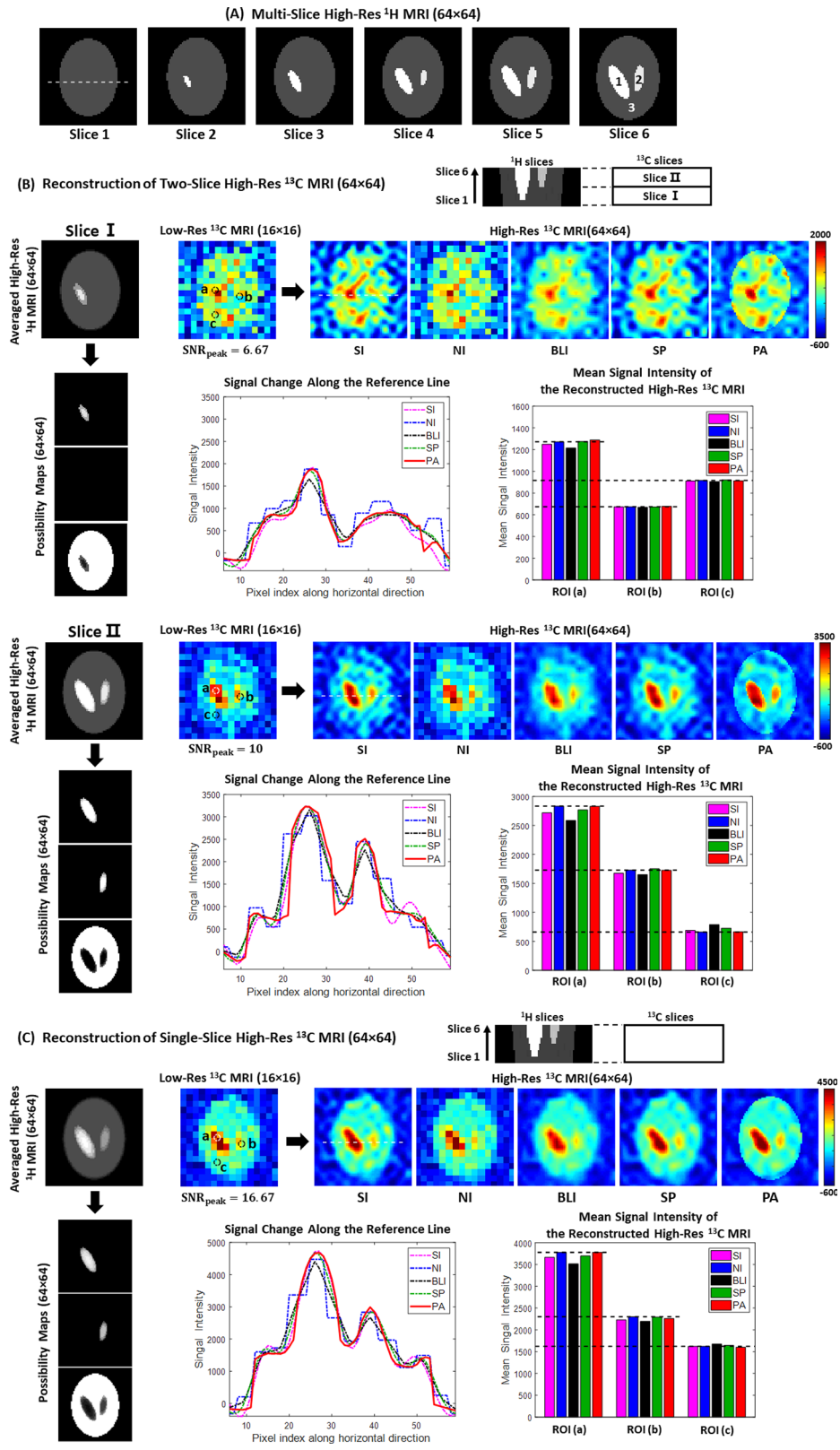

Figure 5. Effect of relative ^{13}C slice thickness to ^{1}H slice on the performance of the PA. A 6-slice 3D digital phantom was generated to represent high-resolution axial multislice ^{1}H images (eg, 0.5-cm slices) (A). To show the case that hyperpolarized ^{13}C images are 3 and 6 times thicker than those of ^{1}H MRI, 2 and 1 low-resolution ^{13}C images were created, respectively, over the slab (eg, 1.5- and 3.0-cm slices). For both cases, the low-resolution ^{13}C images were reconstructed using SI, NI, BLI, SP, and PA. The reconstructed high-resolution ^{13}C images, the signal profiles along the reference lines, and the quantification results are summarized for the ^{13}C images when the slice thickness is 3 (B) and 6 (C) times larger than the ^{1}H slice.

DISCUSSION

In this study, we showed that the patch-based reconstruction algorithm improves spatial resolution and image contrast of ^{13}C images by using *a priori* information obtained from high-resolution ^{1}H MRI. Simulation, phantom, and in vivo studies showed that signal intensity and spatial variation within each compartment were preserved in PA-reconstructed ^{13}C images even when the ^{1}H-based segmentation was suboptimal or

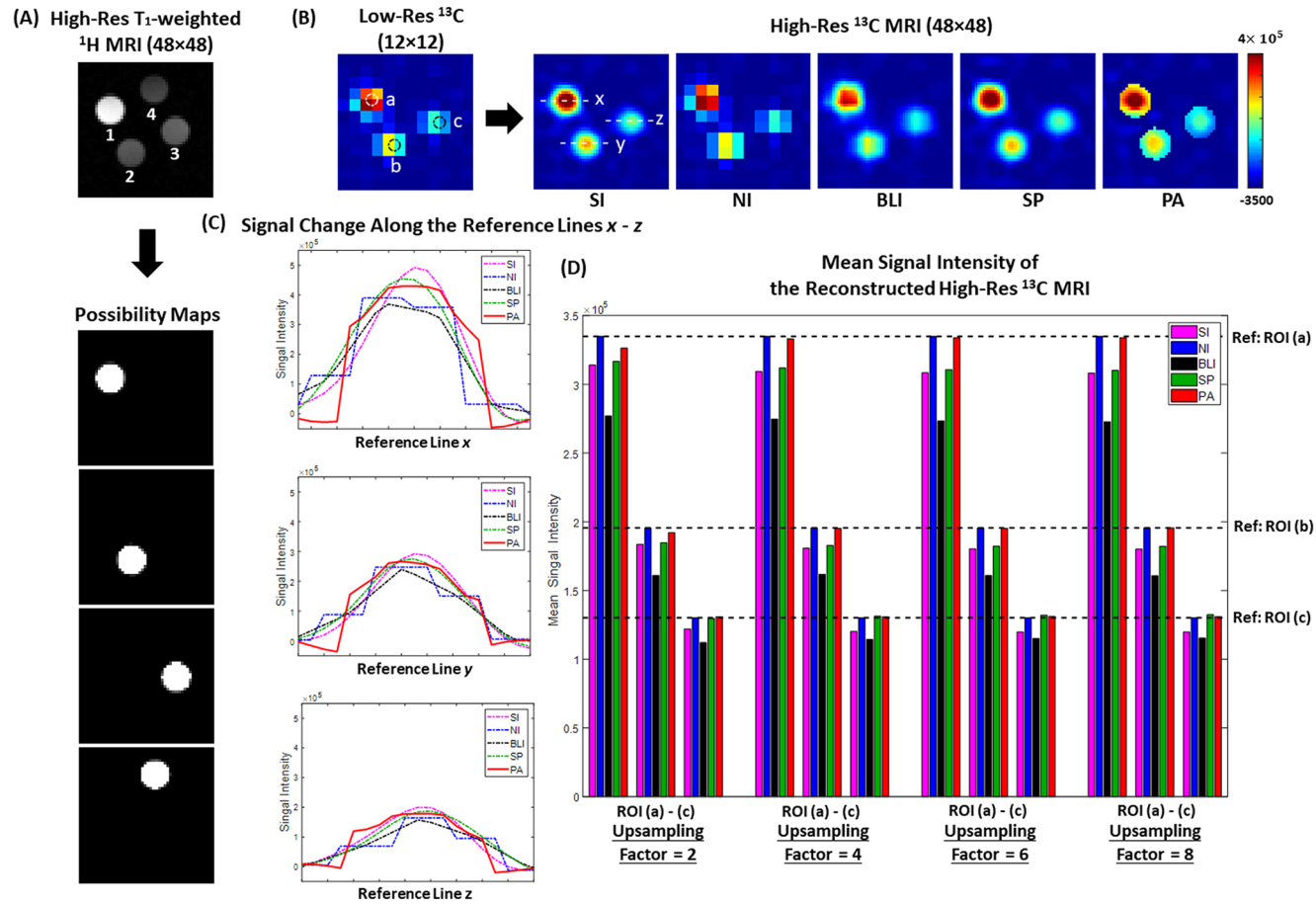

Figure 6. Performance evaluation of PA using magnetic resonance phantoms. Four cylindrical vials were prepared and imaged using ^{1}H/^{13}C dual-tuned radiofrequency coil and a free induction decay CSI sequence. The phantoms #1, #2, and #3 contained ethylene glycol in concentration of 17.7 M, 13.3 M, and 8.8 M, respectively, and phantom #4 was filled with pure water. Possibility maps were calculated from the high-resolution T1-weighted ^{1}H image (A). The acquired low-resolution ^{13}C image was upsampled using SI, NI, BLI, SP, and PA (B). The signal changes along the reference lines *x*, *y*, and *z* (dotted lines in B) (C) and the signal intensities at each vial (ROIs: dotted circles in B), reconstructed with upsampling factors of 2, 4, 6, and 8 (D), showed sharper transition and reliable quantification of PA compared with the other methods.

contaminated to represent the actual ^{13}C distribution. Moreover, the time-resolved dynamic hyperpolarized ^{13}C human brain images showed a consistent performance of PA over temporal changes of the ^{13}C signals.

Consideration of Reconstruction Parameters for Patch-Based Algorithm

The potential mismatch between segmentation and upsampled ^{13}C image increased in proportion to the upsampling factor. Because of the large partial volume effect, the high-resolution segmentation information did not fit into the upsampled image. The impact of this misalignment can be more severe for organs with complex structures and multiple compartments (eg, brain). To maintain the reconstruction accuracy, the upsampling factor was limited to 4 for reconstructing the human brain images (16). However, higher upsampling factors might be eligible for organs with simpler structures without compromising quantification accuracy as the simulation and phantom studies have shown (Figures 2 and 6).

Partial volume effect along the slice thickness on PA performance was also determined. In the simulation, we considered 2 slice thicknesses for ^{13}C images (1.5 and 3.0 cm), considering those reported in the literature (2, 3, 6, 7). The quantification accuracy was not compromised in both cases. With increased slice thickness of ^{13}C image, the calculated possibility maps were exposed to larger potential partial volume effects along the slice direction and blurred edges of compartments, which resulted in limited contrast enhancement in the high-resolution ^{13}C images (Figures 5B and 5C). Nonetheless, the high-resolution images reconstructed from hyperpolarized ^{13}C brain images by using PA showed clear contrast enhancement across CSF and WM, especially for lactate (Figure 8).

Segmentation Strategies for Tissue Compartments

Translation of hyperpolarized ^{13}C technology is still in early stage, and metabolic profiles measured by hyperpolarized ^{13}C-pyruvate in the human brain have not been fully established. As

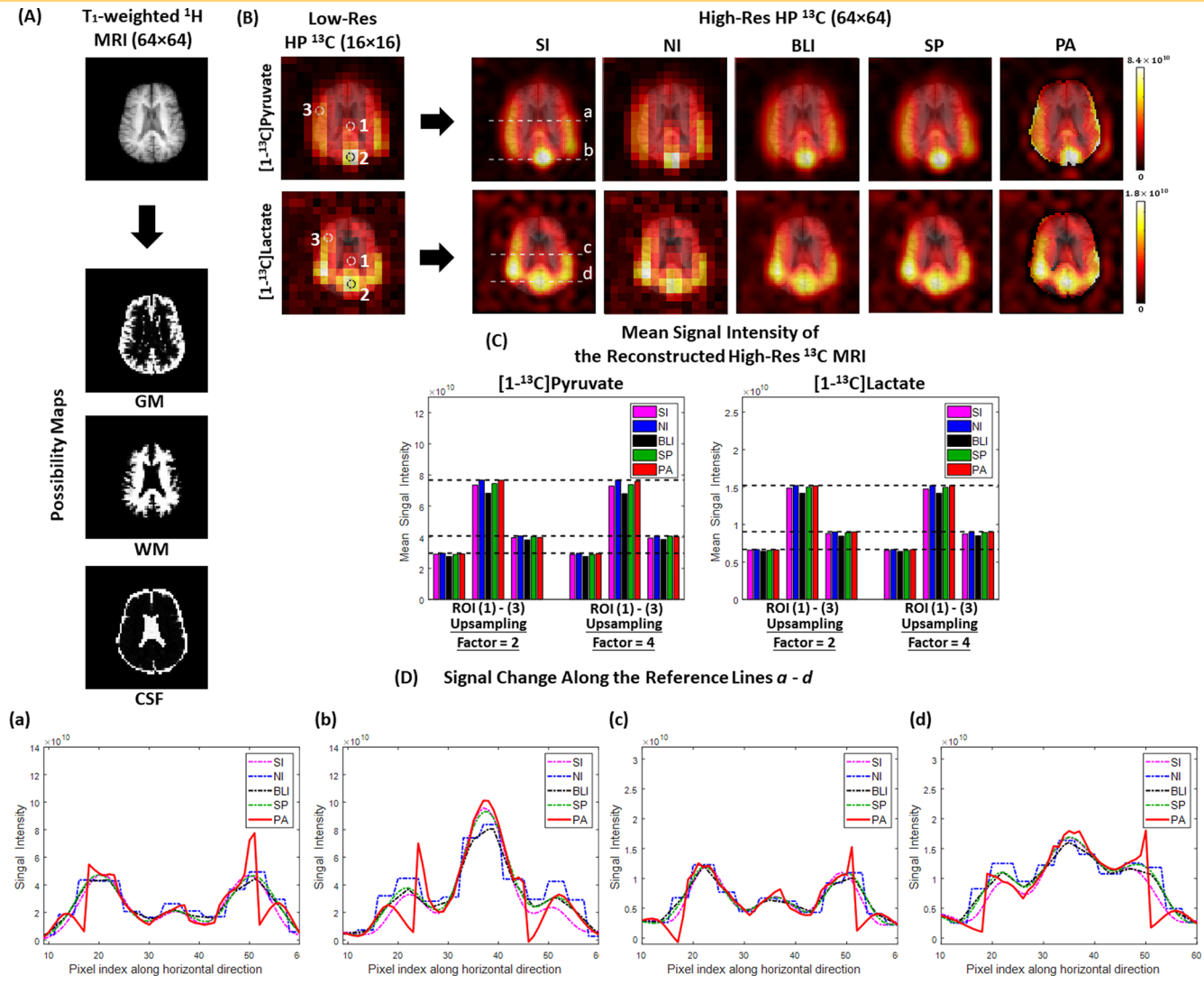

Figure 7. Reconstruction of high-resolution hyperpolarized ^{13}C images of human brain using PA. From the skull-striped T1-weighted ^{1}H image, possibility maps of GM, WM, and CSF were calculated (A). Low-resolution brain images of hyperpolarized [1-^{13}C] pyruvate and [1-^{13}C] lactate were acquired from a healthy subject, then 2- and 4-fold upsampled using SI, NI, BLI, SP, and PA. The images shown are 4-fold upsampled (B). Three distinct ROIs (dotted circles in B) of the brain showed that the signal intensities were reliable for all the ^{13}C-metabolites when reconstructed with upsampling factors of 2 and 4 (C). The signal changes along the reference lines marked in (B) are shown in (D).

this study focused on the verification of PA for hyperpolarized ^{13}C images, a simple model was tested by segmenting the brain tissue to GM, WM, and CSF. Indeed, recent human brain imaging studies using hyperpolarized [1-^{13}C] pyruvate (2, 6) showed larger [1-^{13}C] pyruvate, [1-^{13}C] lactate, and [^{13}C] bicarbonate signals in GM than WM. Although the reconstructed images from PA showed improved intercompartmental contrast and reliable intracompartmental signal distribution, this overly simplified segmentation strategy needs to be further verified and, perhaps, more detailed segmentation models will be required. For instance, Lee et al. (6) reported that the distribution of hyperpolarized [1-^{13}C] lactate, produced from [1-^{13}C] pyruvate, exhibited a consistent pattern when registered to the LPBA40 (LONI Probabilistic Brain Atlas) atlas. Vasculature is another potential compartment, as a large portion of hyperpolarized [1-^{13}C] pyruvate and [1-^{13}C] lactate is preserved in the vasculature. Thus, possibility maps calculated from perfusion images (eg, ASL [Arterial Spin Labeling]) would provide additional detail for reconstructing high-resolution pyruvate and lactate images by PA. If necessary, multimodal imaging–based segmentation strategies can be considered for the optimal PA-based reconstruction (16).

Elevated signals, appearing in the peripherals of PA-reconstructed ^{13}C brain maps (Figure 7, B and D), are likely because of the PA corrected partial volume effect by incorporating the ^{1}H-based segmented information during the reconstruction. This phenomenon was also reported in a previous study (16) and is more noticeable in the pyruvate map. Besides, brighter ^{13}C regions adjacent to dark rims outside of the brain were observed,

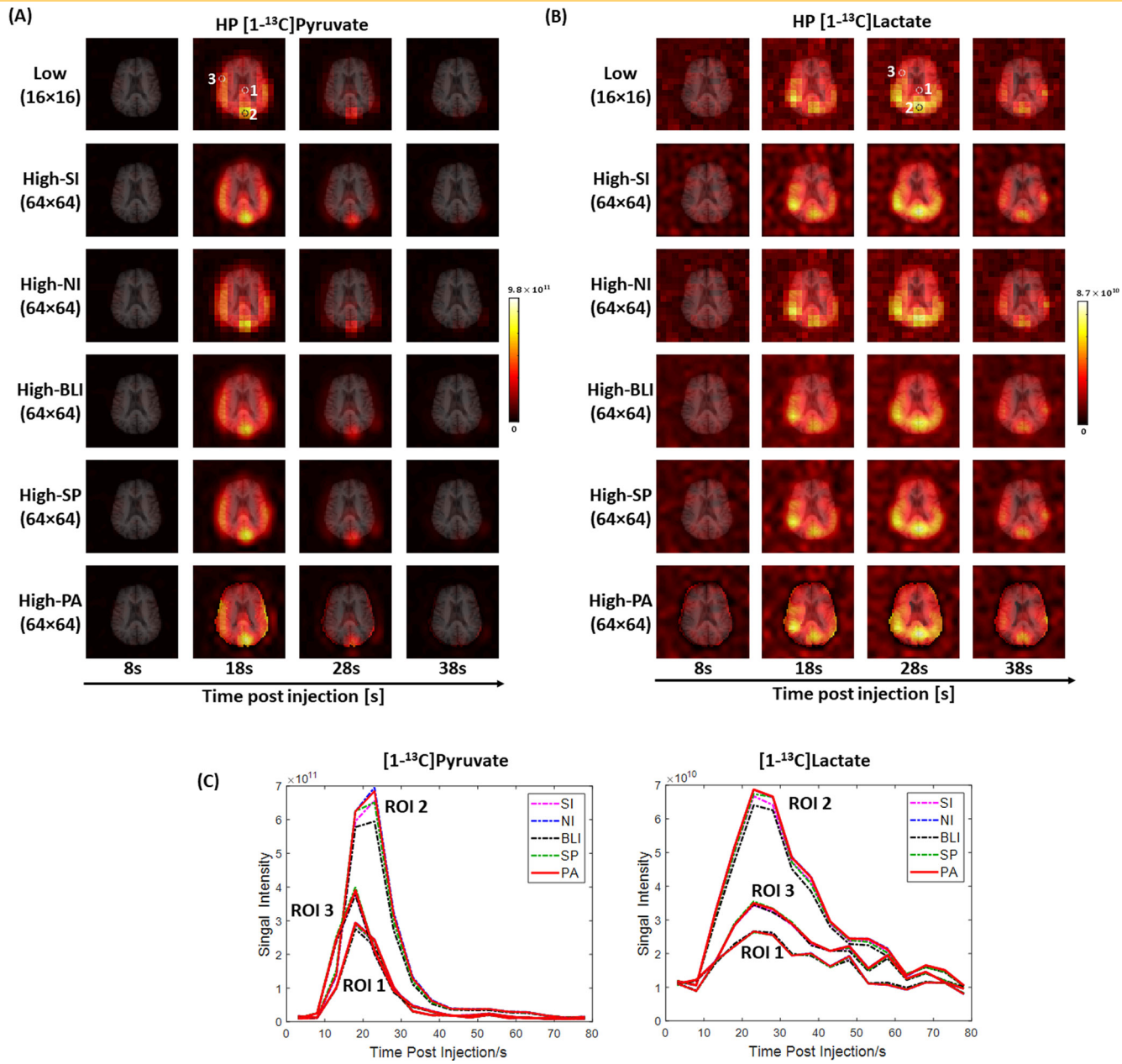

Figure 8. Time-resolved images of hyperpolarized [1-^{13}C] pyruvate (A) and [1-^{13}C] lactate (B) at selective time points from 8 to 38 seconds after the injection were reconstructed to high-resolution images using SI, NI, BLI, SP, and PA. ^{13}C images are overlaid on top of ^{1}H MRI. Temporal changes of pyruvate and lactate in the 3 representative ROIs from CSF, GM, and WM, respectively, were comparable between the reconstructed high-resolution images (C).

implying a misalignment between the segmentation (especially for CSF) and actual ^{13}C signal distribution. In addition to partial volume effect of the low-resolution ^{13}C maps, the mismatch is contributed by insufficient *a priori* knowledge of cerebral compartments. Probability maps with more detailed segmentation strategies may improve the performance of PA at the edges. In particular, inclusion of perfusion map in segmentation will better describe the distribution of pyruvate and lactate in vasculature.

Other Limitations, Potential Improvements, and Future Applications

Because of the characteristics of hyperpolarized ^{13}C molecules and the limited hardware performance used for this study, high-resolution ^{13}C metabolite maps of the human brain could not be acquired. Instead, we compared PA with several other conventional interpolation methods to show the feasibility of PA for reconstructing super-resolution in vivo hyperpolarized ^{13}C images. Potentially, high-resolution in vivo ^{13}C images measured

by accelerated acquisition strategies (eg, parallel imaging, denoising schemes) may be used as ground truth for further evaluation.

Our study shows that proposed PA mainly improves marginal information of the ^{13}C image where segmentation is applied. Within each segmentation, PA shows comparable performance as other interpolation methods. The influence of this limitation could be minor when the ^{13}C images have less complicated segmentation, as shown in simulation and phantom studies. However, for images with intricate compartments such as brain maps, the segmentation strategy should be carefully chosen for optimal performance of PA.

In this study, we assessed PA's performance for improving spatial resolution of single-slice dynamic 2D ^{13}C images. PA can be further developed as a 3D super-resolution method for improving the spatial resolution of volumetric data along the slice-encoding domain as well.

As long as proper segmentations that delineate pathological regions are available, PA can be applied to images with lesions. Indeed, Jain et al. (16) achieved super-resolution spectroscopic ^{1}H brain imaging of patients with multiple sclerosis using PA under the guidance of segmented information from ^{1}H T_1-weighted FLAIR images. Besides, PA is applicable to enhance the hyperpolarized ^{13}C imaging of other organs (such as heart, kidney, and skeletal muscle) with appropriate segmentation strategies. For instance, a compartment for bones would be appropriate when applying PA to hyperpolarized ^{13}C skeletal muscle images, as they do not contain any ^{13}C signal (30).

In conclusion, we proposed a patch-based super-resolution algorithm that exploited high-resolution ^{1}H MRI for reconstructing hyperpolarized ^{13}C images and showed the performance in simulations, phantoms, and hyperpolarized [1-^{13}C] pyruvate images of healthy human brain. Effects of SNR, upsampling factor, segmentation, and slice thickness on the performance of PA were assessed. In addition to improving spatial resolution, the proposed algorithm also enhanced image contrast of ^{13}C images while maintaining the quantification accuracy and intracompartmental signal inhomogeneity.

Supplemental Materials

Supplemental Material : https://doi.org/10.18383/j.tom.2020.00037.sup.01

ACKNOWLEDGMENTS

We appreciate the clinical research team and the supporting staffs of the Advanced Imaging Research Center at UT Southwestern for imaging the volunteers—Craig R. Malloy, MD, Vlad Zaha, MD, Jeff Liticker, PharmD, Crystal E. Harrison, PhD, Lucy Christie, RN, Jeannie Baxter, RN, Kelley Derner, RN, Carol Parcel, RN, Salvador Pena, Edward P. Hackett, MS, Maida Tai, and Richard Martin. We also thank Galen D. Reed, PhD, and Albert P. Chen, PhD, from GE Healthcare.

Funding Support: This study was supported by The Texas Institute for Brain Injury and Repair; Mobility Foundation; National Institutes of Health of the United States (R01 NS107409-01A1, P41 EB015908, S10 OD018468); The Welch Foundation (I-2009-20190330); and UT Dallas Collaborative Biomedical Research Award (UTD 1907789).

Disclosures: The authors have nothing to disclose.

REFERENCES

1. Ardenkjaer-Larsen JH, Fridlund B, Gram A, Hansson G, Hansson L, Lerche MH, Servin R, Thaning M, Golman K. Increase in signal-to-noise ratio of 10,000 times in liquid-state NMR. Proc Natl Acad Sci U S A. 2003;100:10158–10163.
2. Grist JT, McLean MA, Riemer F, Schulte RF, Deen SS, Zaccagna F, Woitek R, Daniels CJ, Kaggie JD, Matys T, Patterson I, Slough R, Gill AB, Chhabra A, Eichenberger R, Laurent M-C, Comment A, Gillard JH, Coles AJ, Tyler DJ, Wilkinson I, Basu B, Lomas DJ, Graves MJ, Brindle KM, Gallagher FA. Quantifying normal human brain metabolism using hyperpolarized 1-13Cpyruvate and magnetic resonance imaging. Neuroimage. 2019;189:171–179.
3. Miloushev VZ, Granlund KL, Boltyanskiy R, Lyashchenko SK, DeAngelis LM, Mellinghoff IK, Brennan CW, Tabar V, Yang TJ, Holodny AI, Sosa RE, Guo YW, Chen AP, Tropp J, Robb F, Keshari KR. Metabolic Imaging of the human brain with hyperpolarized 13C pyruvate demonstrates 13C lactate production in brain tumor patients. Cancer Res. 2018;78:3755–3760.
4. Cunningham CH, Lau JYC, Chen AP, Geraghty BJ, Perks WJ, Roifman I, Wright GA, Connelly KA. Hyperpolarized 13C metabolic MRI of the human heart: initial experience. Circ Res. 2016;119:1177–1182.
5. Nelson SJ, Kurhanewicz J, Vigneron DB, Larson PEZ, Harzstark AL, Ferrone M, van Criekinge M, Chang JW, Bok R, Park I, Reed G, Carvajal L, Small EJ, Munster P, Weinberg VK, Ardenkjaer-Larsen JH, Chen AP, Hurd RE, Odegardstuen L-I, Robb FJ, Tropp J, Murray JA. Metabolic imaging of patients with prostate cancer using hyperpolarized 1-^{13}Cpyruvate. Sci Transl Med. 2013;5:198ra108.
6. Lee CY, Soliman H, Geraghty BJ, Chen AP, Connelly KA, Endre R, Perks WJ, Heyn C, Black SE, Cunningham CH. Lactate topography of the human brain using hyperpolarized 13C-MRI. Neuroimage. 2020;204:116202.
7. Park I, Larson PEZ, Gordon JW, Carvajal L, Chen H-Y, Bok R, Van Criekinge M, Ferrone M, Slater JB, Xu D, Kurhanewicz J, Vigneron DB, Chang S, Nelson SJ. Development of methods and feasibility of using hyperpolarized carbon-13 imaging data for evaluating brain metabolism in patient studies. Magn Reson Med. 2018;80:864–873.
8. Lau AZ, Chen AP, Hurd RE, Cunningham CH. Spectral-spatial excitation for rapid imaging of DNP compounds. NMR Biomed. 2011;24:988–996.
9. Cunningham CH, Vigneron DB, Chen AP, Xu D, Nelson SJ, Hurd RE, Kelley DA, Pauly JM. Design of flyback echo-planar readout gradients for magnetic resonance spectroscopic imaging. Magn Reson Med. 2005;54:1286–1289.
10. Wiesinger F, Weidl E, Menzel MI, Janich MA, Khegai O, Glaser SJ, Haase A, Schwaiger M, Schulte RF. IDEAL spiral CSI for dynamic metabolic MR imaging of hyperpolarized 1-13Cpyruvate. Magn Reson Med. 2012;68:8–16.
11. Larkman DJ, Nunes RG. Parallel magnetic resonance imaging. Phys Med Biol. 2007;52:R15–55.
12. Lustig M, Donoho D, Pauly JM. Sparse MRI: the application of compressed sensing for rapid MR imaging. Magn Reson Med. 2007;58:1182–1195.
13. Arunachalam A, Whitt D, Fish K, Giaquinto R, Piel J, Watkins R, Hancu I. Accelerated spectroscopic imaging of hyperpolarized C-13 pyruvate using SENSE parallel imaging. NMR Biomed. 2009;22:867–873.
14. Geraghty BJ, Lau JYC, Chen AP, Cunningham CH. Accelerated 3D echo-planar imaging with compressed sensing for time-resolved hyperpolarized 13 C studies. Magn Reson Med. 2017;77:538–546.
15. Kasten J, Klauser A, Lazeyras F, van de Ville D. Magnetic resonance spectroscopic imaging at superresolution: overview and perspectives. J Magn Reson. 2016;263:193–208.
16. Jain S, Sima DM, Nezhad Hangel SF, Bogner G, Williams W, van Huffel S, Maes S, Smeets FD. Patch-based super-resolution of MR spectroscopic images: application to multiple sclerosis. Front Neurosci. 2017;11:13
17. Hu X, Levin DN, Lauterbur PC, Spraggins T. SLIM: spectral localization by imaging. Magn Reson Med. 1988;8:314–322.
18. Haldar JP, Hernando D, Song S-K, Liang Z-P. Anatomically constrained reconstruction from noisy data. Magn Reson Med. 2008;59:810–818.
19. Farkash G, Markovic S, Novakovic M, Frydman L. Enhanced hyperpolarized chemical shift imaging based on a priori segmented information. Magn Reson Med. 2019;81:3080–3093.
20. Kornak J, Young K, Soher BJ, Maudsley AA. Bayesian k-space-time reconstruction of MR spectroscopic imaging for enhanced resolution. IEEE Trans Med Imaging. 2010;29:1333–1350.

21. Manjón JV, Coupé P, Buades A, Collins DL, Robles M. MRI superresolution using self-similarity and image priors. Int J Biomed Imaging. 2010;2010:425891.
22. Rousseau F. A non-local approach for image super-resolution using intermodality priors. Med Image Anal. 2010;14:594–605.
23. Coupé P, Manjón JV, Chamberland M, Descoteaux M, Hiba B. Collaborative patch-based super-resolution for diffusion-weighted images. Neuroimage. 2013;83:245–261.
24. Manjón JV, Coupé P, Buades A, Fonov V, Louis Collins D, Robles M. Non-local MRI upsampling. Med Image Anal. 2010;14:784–792.
25. Ma J, Hashoian R, Sun C, Wright S, Ivanishev A, Lenkinski R, Malloy C, Chen A, Park JM. Development of 1H/13C RF head coil for hyperpolarized 13C imaging of human brain. Proceedings of the 27th ISMRM, Montreal, Canada;#568.
26. Park JM, Liticker J, Harrison CE, Reed GD, Hever T, Ma J, Martin R, Mayer D, Hashoian RS, Madden CJ, Pinho MC, Malloy CR. Feasibility and reproducibility of imaging brain metabolism using hyperpolarized 13C pyruvate in humans. Proceedings of the 27th ISMRM, Montreal, Canada;#4311.
27. Park JM, Josan S, Jang T, Merchant M, Yen Y-F, Hurd RE, Recht L, Spielman DM, Mayer D. Kinetics in C6 rat glioma model using magnetic resonance spectroscopic imaging of hyperpolarized 1-(13)C pyruvate. Magn Reson Med. 2012;68:1886–1893.
28. Smith SM. Fast robust automated brain extraction. Hum Brain Mapp. 2002;17:143–155.
29. Zhang Y, Brady M, Smith S. Segmentation of brain MR images through a hidden Markov random field model and the expectation-maximization algorithm. IEEE Trans Med Imaging. 2001;20:45–57.
30. Park JM, Josan S, Mayer D, Hurd RE, Chung Y, Bendahan D, Spielman DM, Jue T. Hyperpolarized 13C NMR observation of lactate kinetics in skeletal muscle. J Exp Biol. 2015;218:3308–3318.